ACCSCIENCE PUBLISHING

International Journal of Bioprinting

RESEARCH ARTICLE

Bionic trabecular titanium alloy scaffolds produced by selective laser melting enhancement of bone and vascular regeneration through Schwann cell-mediated mechanotransduction

Jiqing Wang[1], Aofei Xu[1], Weiying Zhang[1], Xingda Huang[1], Xuezhe Han[1], Shuming Li[1], Dezhi Wang[2]*, and Jiantao Liu[1]*

[1]Department of Orthopedics, The First Affiliated Hospital of Xi'an Jiaotong University, Xi'an, Shaanxi, China

[2]Department of Anesthesiology, Honghui Hospital, Xi'an Jiaotong University, Xi'an, Shaanxi, China

***Corresponding authors:**
Dezhi Wang
(derver8479@sina.com)

Jiantao Liu
(liujiantao2010xjtu@163.com)

Citation: Wang J, Xu A, Zhang W, *et al.* Bionic trabecular titanium alloy scaffolds produced by selective laser melting enhance bone and vascular regeneration through Schwann cell-mediated mechanotransduction. *Int J Bioprint.* 2025;11(3):185-198. doi: 10.36922/IJB025120092

Received: March 17, 2025
Revised: April 15, 2025
Accepted: May 2, 2025
Published Online: May 2, 2025

Abstract

Using selective laser melting, a metal three-dimensional (3D) printing technique, we developed bionic trabecular titanium alloy scaffolds with a micro–nano composite porous structure to address the limitations of traditional titanium implants. By integrating bionic design principles with advanced metal 3D printing strategies, these scaffolds mimic the trabecular network of cancellous bone, reducing elastic modulus (to ~4 GPa) and mitigating stress shielding. The bioprinted scaffolds exhibited enhanced surface properties that promoted Schwann cell (SC) adhesion, elongation, and spindle-like morphology, forming cellular networks along the microporous architecture. In contrast, SCs on solid titanium scaffolds displayed a flattened morphology with limited functionality. Transcriptomic analysis revealed that the scaffold's micro–nano structure regulated SC behavior via the focal adhesion kinase-mitogen-activated protein kinase mechanotransduction pathway, enhancing the secretion of pro-osteogenic (e.g., platelet-derived growth factor with two A subunits) and pro-angiogenic (e.g., vascular endothelial growth factor) factors. Trabecular-like scaffold-conditioned medium significantly accelerated bone marrow mesenchymal stem cell proliferation, osteogenic differentiation, and endothelial cell angiogenesis, achieving a 36% higher healing rate compared to controls. While *in vivo* validation remains essential, our *in vitro* model isolates SC-driven mechanisms, avoiding systemic confounders. This study highlights the potential of 3D bioprinted scaffolds for personalized bone defect repair, offering a biomechanically and biologically optimized solution to enhance osseointegration.

Keywords: 3D printing; Bone regeneration; Mechanotransduction; Schwann cells; Selective laser melting; Titanium alloy

1. Introduction

Bone defects caused by tumors, fractures, and degenerative diseases pose a significant threat to human health.[1,2] Titanium alloys, due to their superior mechanical and biological properties, have been extensively used in the reconstruction of bone defects.[3] However, long-term clinical follow-ups have revealed complications such as implant loosening and displacement, particularly in patients with osteoporosis, where the incidence is markedly higher. These issues are attributed to the high elastic modulus of titanium alloys (~110 GPa), which greatly exceeds that of natural cortical bone (17–20 GPa) and cancellous bone (~4 GPa). This substantial discrepancy results in a "stress shielding" effect, leading to bone resorption.[4] Furthermore, titanium alloys are bioinert, exhibiting limited bioactivity and making integration with surrounding bone tissue challenging after implantation.[5] Addressing these issues, particularly the mismatch in elastic modulus and the promotion of osseointegration, is critical for the success of titanium implants.

Recent advancements in metal three-dimensional (3D) printing technologies, particularly selective laser melting (SLM), have revolutionized the fabrication of porous titanium alloys, enabling precise control over their biomechanical and osseointegration properties.[6] As demonstrated in recent metal 3D printing studies,[7,8] SLM allows the creation of micro–nano composite structures that closely replicate the architecture of natural trabecular bone. Compared to dense counterparts, these bioprinted porous designs not only reduce the elastic modulus of titanium implants (thereby improving biomechanical compatibility) but also mitigate the "stress shielding" phenomenon.[9] Mimicking the trabecular bone architecture through the creation of bionic structures has the potential to reduce the elastic modulus of titanium alloys and enhance their osseointegration performance.[10]

SCs, the primary glial cells of the peripheral nervous system, play a pivotal role in modulating the bone repair microenvironment.[11] Recent research has highlighted their regulatory function in bone regeneration through the secretion of paracrine factors such as brain-derived neurotrophic factor (BDNF), nerve growth factor (NGF), and platelet-derived growth factor with two A subunits (PDGF-AA). These factors modulate the behavior of osteoblasts and endothelial cells, thereby promoting both bone repair and vascularization.[12] The ability of SCs to respond to mechanical stimuli is particularly relevant in the context of implant materials, as surface properties significantly influence SC function.[13] SCs are sensitive to changes in surface morphology and roughness, with studies showing that textured surfaces, such as those created by sandblasting or hydroxyapatite coating, enhance SC behavior.[14] These findings suggest that the surface morphology of biomaterials plays a key role in regulating SC function.

In this study, we investigate the mechanobiological mechanisms by which bionic trabecular titanium alloy scaffolds regulate SC functions. We hypothesize that scaffolds with micro–nano composite porous structures promote SC adhesion, proliferation, and function via mechanotransduction pathways, specifically through the focal adhesion kinase-mitogen-activated protein kinase (FAK-MAPK) signaling axis. This research aims to elucidate how these scaffolds modulate the bone repair microenvironment to enhance both bone and vascular regeneration, ultimately improving the osseointegration performance of titanium implants. Our findings offer a novel approach for advancing the integration of titanium implants in bone defect repair.

2. Methods

2.1. Immunofluorescence observation of bone repair

Adult male Sprague–Dawley (SD) rats were anesthetized to establish a tibial fracture model (n = 15). Tibial specimens were harvested at 7, 14, 21, 28, and 35 days post-surgery following euthanasia. The specimens were fixed with paraformaldehyde, decalcified using ethylenediaminetetraacetic acid (EDTA), embedded in paraffin, and sectioned for histological analysis. SCs and nerve axons were specifically labeled using primary antibodies S100 calcium-binding protein B (S100β; 1:1000; bsm-10832M; Bioss, China) and β III-tubulin (1:1000; bs-4512R, Bioss, China), respectively. Fluorescein isothiocyanate-conjugated goat anti-mouse IgG (1:400; GB25301, Servicebio, Wuhan, China) or cyanine5-conjugated goat anti-rabbit IgG (1:400; GB27303, Servicebio, Wuhan, China) were used as secondary antibodies and incubated in the dark at room temperature for 50 min. Subsequently, nuclei were counterstained with 4',6-diamidino-2-phenylindole (DAPI) in the dark at room temperature for 10 min. Fluorescence imaging was conducted using a Nikon inverted fluorescence microscope.

2.2. Fabrication of bionic trabecular scaffolds via 3D bioprinting

A bionic trabecular 3D model with 65% porosity and an average pore size of 550 μm was designed using computer-aided software (Figure 1A-a). The scaffolds were fabricated via SLM, a metal additive manufacturing technique, using optimized parameters: laser power of 200 W, scanning speed of 800 mm/s, and layer thickness of 30 μm (EOS M290 system, EOS GmbH, Germany). All process

parameters adhered to ISO/ASTM 52900 standards for additive manufacturing, ensuring reproducibility and structural fidelity. After printing, the titanium alloy scaffolds underwent a dealloying process to form micro–nano composite structures. The process involved several steps: first, the printed scaffolds were immersed in a sodium chloride solution and subjected to high-temperature heat treatment at 700 °C for 2 h, facilitating the selective leaching of certain elements from the alloy and generating a porous structure with micro/nano features. Next, the scaffolds were treated with an acidic solution containing hydrochloric acid and nitric acid to induce surface corrosion, forming the desired micro–nano composite texture. This corrosion treatment created nanopores and irregular surface textures, significantly increasing surface area and roughness, which is beneficial for enhancing cell adhesion, proliferation, and differentiation. Finally, the scaffolds were thoroughly washed with deionized water to remove residual chemicals and sterilized by autoclaving following treatment with 70% ethanol to ensure aseptic conditions for cell culture experiments (Figure 1A).

2.3. Isolation and culture of cells

Four-week-old SD rats (n = 5) were euthanized with an overdose of pentobarbital, and the sciatic nerves were aseptically isolated following disinfection with 75% ethanol. The nerves were digested with 3 mg/mL collagenase (DY40127, Deeyee, China) in a 37 °C incubator for 30 min. After centrifugation, the supernatant was removed, and the pellet was resuspended in trypsin/EDTA (25300054, Thermo Scientific, USA) and digested at 37 °C for 10 min. Digestion was then terminated, and after a second centrifugation, the supernatant was discarded. The pellet was resuspended in complete medium (Dulbecco's Modified Eagle's Medium [DMEM; PM150210, Servicebio, China] + 10% fetal bovine serum [FBS]), filtered through a cell strainer, and seeded into culture dishes. After overnight incubation, the medium was replaced with a complete medium containing 10 μM cytarabine (HY-13605, MedChemExpress, USA) under light-protected conditions. Two days later, the medium was replaced with a complete medium supplemented with 2 μM Forskolin (HY-15371, MedChemExpress, USA) and 10

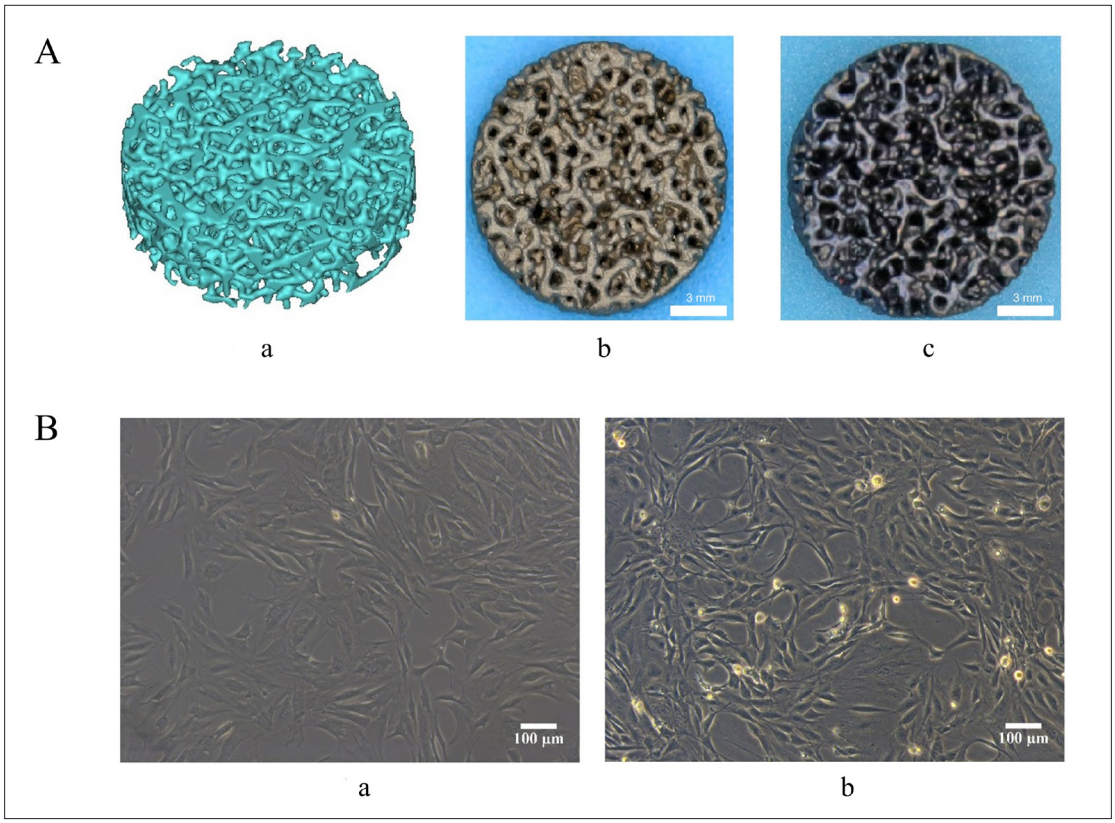

Figure 1. Preparation of bionic trabecular titanium alloy scaffolds using metal 3D printing and extraction of primary rat cells. (A) The fabrication process of bionic trabecular scaffolds: a. 3D model of trabecular-like structure, b. Selective laser melting-printed scaffold with micropores, c. 3D-bioprinted scaffold with micro–nano composite pores. Scale bar = 3 mm. Panels b and c were captured using a digital camera under natural lighting conditions. (B) Extraction of primary rat cells: a. Schwann cells, b. Bone marrow-derived mesenchymal stem cells. Scale bar = 100 μm; Magnification = 200×. Abbreviation: 3D, three-dimensional.

ng/mL neuregulin (HY-P7365, MedChemExpress, USA) to stimulate the rapid proliferation of SCs (Figure 1B-a).

Femurs and tibias were collected from rats, and surrounding tendons and muscles were removed. The bones were repeatedly washed with sterile phosphate-buffered saline (PBS), soaked in minimal essential medium Eagle-alpha modification medium (α-MEM; G4554, Servicebio, China), and the epiphyseal ends of the femurs and tibias were removed. Bone marrow was flushed out with DMEM medium using a five-gauge syringe and dissociated into a single-cell suspension by repeated pipetting. The suspension was filtered through a cell strainer and centrifuged at 1000 rpm for 5 min. After the supernatant was discarded, the pellet was resuspended in DMEM medium containing 10% FBS (FSP500, ExCell Bio, China) and seeded into culture dishes. The dishes were incubated at 37 °C in a 5% CO_2 atmosphere. Non-adherent cells were removed by changing the medium over the first 3 days, leaving behind adherent bone marrow-derived mesenchymal stem cells (BMSCs) (Figure 1B-b).

2.4. Identification of SCs

To ensure the purity of SCs for subsequent experiments, immunofluorescence staining was performed. SCs were seeded at a density of 5000 cells per well in 24-well plates containing sterilized round coverslips at the bottom of each well. After 48–72 h of culture in complete SC medium (DMEM + 10% FBS, supplemented with 2 μM Forskolin and 10 ng/mL neuregulin), cells were gently washed three times with PBS to remove non-adherent cells and then fixed with 4% paraformaldehyde at room temperature for 15 min.

Following fixation, cells were permeabilized with 0.2% Triton X-100 in PBS for 10 min and subsequently blocked with 5% bovine serum albumin for 30 min to minimize non-specific binding. The primary antibody against S100β (1:200; bsm-10832M, Bioss, China) was added and incubated overnight at 4 °C. The next day, after three washes with PBS, cells were incubated for 1 h at room temperature in the dark with Alexa Fluor 488-conjugated goat anti-mouse IgG (1:400; GB25301, Servicebio, Wuhan, China) as the secondary antibody. Nuclei were counterstained with DAPI (1 μg/mL) for 5 min at room temperature, followed by three additional PBS washes. Finally, coverslips were mounted onto glass slides using an anti-fade mounting medium and sealed.

Fluorescence imaging was performed using a Nikon inverted fluorescence microscope. The percentage of S100β-positive cells (green fluorescence) was calculated based on five randomly selected fields per coverslip. Only cells showing both DAPI-stained nuclei and S100β-positive cytoplasm were counted as SCs. Quantitative analysis indicated that more than 95% of the cells were S100β-positive, suggesting that the isolated SCs were of high purity and suitable for subsequent experiments.

2.5. Transcriptomic sequencing

SCs were seeded onto bionic trabecular and solid titanium alloy scaffolds and cultured in DMEM medium supplemented with 10% FBS for 3 days. Total RNA was extracted from the cells for transcriptomic sequencing. Differential gene expression analysis was performed, including a cluster of orthologous genes (COG) classification, Kyoto Encyclopedia of Genes and Genomes (KEGG) pathway analysis, and Gene Ontology (GO) enrichment analysis, to explore the molecular mechanisms through which bionic trabecular titanium alloy scaffolds regulate SC function.

2.6. Morphological observation of SCs on titanium alloy scaffolds

Smooth-surfaced solid titanium alloy scaffolds were used as controls. Both bionic trabecular and solid titanium alloy scaffolds were sequentially sonicated in deionized water, acetone, 95% ethanol, and again in deionized water for 30 min each. They were then sterilized via high-temperature autoclaving for subsequent cell experiments. The scaffolds were placed into sterile 24-well plates, with three replicates per scaffold type. SCs at a density of 1×10^5 cells/mL (P4) were seeded into the wells containing scaffolds at 1 mL per well. Cells were cultured in a complete medium (DMEM + 10% FBS) in a 37 °C, 5% CO_2 incubator for 3 days. DAPI/phalloidin staining was performed to observe SC morphology on the different scaffolds, and immunofluorescence assays were conducted for further morphological analysis.

2.7. Proliferation and osteogenic differentiation of bone marrow-derived mesenchymal stem cells

SCs were seeded onto bionic trabecular and solid titanium alloy scaffolds. After 3 days of culture, the supernatants were collected and mixed with BMSC culture medium (α-MEM + 10% FBS) at a 1:1 ratio to prepare the conditioned medium. The medium derived from SCs cultured on trabecular-like scaffolds was termed trabecular-like scaffold-conditioned medium (TL-CM), while that from SCs cultured on solid titanium scaffolds was termed solid scaffold-conditioned medium (Solid-CM). BMSCs were cultured in the conditioned medium for a designated time, and cell proliferation was assessed using a Cell Counting Kit-8 (CCK-8; C0038, Beyotime, China). Alkaline phosphatase (ALP) activity was evaluated using an ALP assay kit (P0321S, Beyotime, China), while ALP expression and calcium deposition were assessed using an azo coupling ALP staining kit (S0100, Bioss, China)

and Alizarin Red staining (G1452, Solarbio, China), respectively. Quantitative analysis of calcium deposition was performed using 10% cetylpyridinium chloride (6004-24-6, Sigma, USA). Additionally, reverse transcription polymerase chain reaction (RT-PCR) was used to measure the expression levels of osteogenic-related genes, including *Alp*, osteocalcin (*Ocn*), and runt-related transcription factor 2 (*Runx2*). Primer sequences are listed in Table 1.

2.8. Angiogenesis assay

To investigate the effect of different titanium alloy scaffolds on SC-mediated endothelial cell angiogenesis, an angiogenesis assay was conducted. The procedure was as follows: 3 days prior to the experiment, conditioned medium was prepared by mixing the supernatants of SCs cultured on different titanium alloy scaffolds with endothelial cell medium (CC-3202, Lonza, China) at a 1:1 ratio. Endothelial cells were cultured in this conditioned medium. One day before the assay, Matrigel (HY-K6002, MedChemExpress, USA), 10 μL and 1 mL pipette tips, and 24-well plates were pre-cooled at 4 °C overnight. On the day of the experiment, 10 μL of Matrigel was evenly spread in the pre-chilled 24-well plates using a pre-cooled 1 mL pipette tip. After the Matrigel solidified, endothelial cells were digested and resuspended in the conditioned medium at a concentration of 1×10^5 cells/well. Cells were seeded into the 24-well plates with three replicates per condition and cultured for 6 h in an incubator. Angiogenic activity was assessed under an optical microscope (10× magnification), and images were analyzed using the Angiogenesis Analyzer plugin in ImageJ.

2.9. Endothelial cell migration assay

To evaluate the ability of SCs, influenced by different titanium alloy scaffolds, to promote endothelial cell migration, a scratch wound healing assay was performed. This assay involves creating a scratch in a confluent monolayer of cells and monitoring cell migration into the scratch area over time. The procedure was as follows: 3 days prior to the experiment, a conditioned medium was prepared as described in the angiogenesis assay. On the day of the experiment, horizontal reference lines were drawn on the back of 6-well plates. Logarithmic-phase endothelial cells were digested with trypsin and resuspended in the conditioned medium as a single-cell suspension at a density of 5×10^5 cells/well. Cells were seeded into the 6-well plates and incubated overnight at 37 °C in 5% CO_2 to achieve full confluence. A 1 mL pipette tip was used to create a scratch perpendicular to the marked lines. After scratching, the medium was removed, and the wells were washed three times with sterile PBS. Serum-free endothelial cell medium was then added. Images of the scratches were captured at 0, 12, and 24 h under an optical microscope (5× magnification), and scratch closure was quantified using ImageJ. The scratch healing rates were calculated using **Equation I**:

$$\text{Scratch healing rate (\%)} = \cdot \frac{\text{Area at 0 h} - \text{Area at 12 (or 24) h}}{\text{Area at 0 h}} \times 100\% \quad \text{(I)}$$

2.10. ELISA assay

The expression levels of BDNF, NGF, and PDGF-AA were measured in the bionic trabecular group, solid scaffold group, and blank control group using enzyme-linked immunosorbent assay (ELISA). Commercial ELISA kits from ShanDeZhiYuan were used according to the manufacturer's instructions, including RX2D306406 for rat BDNF, RX302374R for rat NGF, and RX300051R for rat PDGF-AA. Samples were diluted and added to 96-well plates, followed by incubation, washing, and substrate reaction. Optical density values were measured at 450 nm. Protein concentrations were calculated using standard curves, and statistical significance was assessed using a one-way analysis of variance, with $p < 0.05$ considered statistically significant.

2.11. Statistical methods

Independent sample *t*-tests were used for statistical analysis. If the data did not meet the assumption of normal distribution, non-parametric methods such as the Kruskal–Wallis *H* test or Mann–Whitney *U* test were applied. All statistical analyses were performed using GraphPad Prism 8 (GraphPad Software, USA) or SPSS Statistics 25 (IBM, USA). Statistical significance was defined as $p < 0.05$.

Table 1. Forward and reverse primer sequences for reverse transcription polymerase chain reaction

Gene	Upper primers	Lower primers
Alp	5'-GGCACCTGCCTTACCAACTCT-3'	5'-GTTGTGGTGTAGCTGGCCCTTA-3'
Ocn	5'-ACAGGCTTCCTAGAACAAGGGC-3'	5'-AAGAACTCAAACATACGGGCAA-3'
Runx2	5'-ATGACACTGCCACCTCTGACTTCT-3'	5'AGGGATGAAATGCTTGGGAACT-3'
Gapdh	5'-CCTCGTCCCGTAGACAAAATG-3'	5'-TGAGGTCAATGAAGGGGTCGT-3'

3. Results

3.1. Neural regulation of bone repair

Immunofluorescence staining of rat tibial specimens revealed a significant distribution of nerve fibers (indicated by red fluorescence) in both non-fractured and healing fracture samples, confirming that bone is a tissue rich in nerve fibers. In non-fractured samples, no aggregation of SCs, indicated by green fluorescence, was observed. However, in fracture samples, substantial SC aggregation was detected, with their numbers steadily increasing during the first 4 weeks post-fracture and decreasing thereafter (Figure 2A). These findings suggest that SCs are widely present during the early stages of bone healing and play a crucial role in regulating bone repair.

3.2. Morphological characteristics of bionic trabecular titanium alloy scaffolds

Scanning electron microscopy analysis revealed that the pore size distribution of the micro–nano structure ranged from 200 to 500 μm, with a porosity of approximately 65%, closely resembling the pore architecture of natural trabecular bone. This structure effectively mimics the microenvironment of natural bone, supporting cell adhesion, proliferation, and differentiation (Figure 2B).

3.3. Immunofluorescence identification of SCs

To verify the purity of SCs, immunofluorescence staining for S100β was conducted. The majority of cells exhibited positive S100β expression, with nuclei counterstained by DAPI (Figure 2C). Quantitative analysis indicated that over 95% of the cells were S100β-positive, suggesting that the isolated SCs were of high purity and suitable for subsequent experiments.

3.4. Transcriptomic sequencing

Transcriptomic sequencing identified 419 differentially expressed genes (DEGs) in SCs cultured on the bionic trabecular titanium alloy scaffold, including 52 upregulated and 367 downregulated genes (Figure 3A). COG classification analysis revealed that these DEGs play critical roles in signal transduction mechanisms (Figure 3B). KEGG pathway annotation showed that the DEGs were primarily enriched in cellular process-related pathways such as focal adhesion and cytoskeletal regulation (Figure 3C). GO enrichment analysis further indicated that these genes are significantly involved in gene transcription regulation (Figure 3D). These findings suggest that the bionic trabecular titanium alloy scaffold modulates SC function through mechanotransduction pathways, including focal adhesion, cytoskeletal regulation, and gene transcription. Further enrichment analysis highlighted the pivotal role of the focal adhesion pathway in mediating SC adhesion to the scaffold. This pathway activates the MAPK/extracellular signal-regulated kinase (ERK) signaling cascade, enhancing the expression and secretion of neurotrophic and angiogenic factors, thereby optimizing the bone repair microenvironment.

3.5. Morphological observation of SCs on titanium alloy scaffolds

After 3 days of culture, DAPI/phalloidin staining revealed that SCs successfully adhered to and proliferated on both types of titanium alloy scaffolds, as observed under an inverted fluorescence microscope. Nuclei stained with DAPI appeared blue, while cytoskeleton F-actin stained with phalloidin appeared red (Figure 4A). On the bionic trabecular titanium alloy scaffold, SCs exhibited excellent adhesion and elongation, with a spindle-shaped morphology. Cells aligned along the microporous structure of the scaffold, forming distinct cellular networks. Cellular protrusions extended into the scaffold pores, demonstrating that the 3D porous architecture of the scaffold supports cell attachment.

In contrast, SCs on the solid titanium alloy scaffold also adhered and grew but displayed a more flattened morphology, with reduced elongation and fewer intercellular connections. Immunofluorescence staining further showed that SCs on the bionic trabecular titanium alloy scaffold had significantly greater nuclear localization of phosphorylated ERK (p-ERK) (Figure 4B). These findings suggest that the surface morphology of the bionic trabecular scaffold may influence p-ERK nuclear localization through a mechanotransduction pathway, thereby modulating SC functions.

3.6. Proliferation and osteogenic differentiation of bone marrow-derived mesenchymal stem cells

The proliferation assay showed that BMSCs cultured in TL-CM for 3 and 5 days exhibited significantly higher proliferation rates compared to those in Solid-CM ($p < 0.05$). Statistical significance is indicated by $p < 0.05$ between the two groups (Figure 4C). On day 5, the proliferation rate in the TL-CM group was approximately 36% higher than in the Solid-CM group.

On days 7 and 14, ALP activity in the TL-CM group was significantly higher than in the Solid-CM group ($p < 0.05$) (Figure 4D). ALP staining further confirmed increased ALP expression in the TL-CM group, as indicated by more intense purple staining (Figure 4D). On day 30, Alizarin Red staining revealed that the TL-CM group formed more and larger mineralized nodules compared to the Solid-CM group (Figure 4D).

Gene expression analysis via RT-PCR on days 7 and 14 demonstrated that the mRNA levels of osteogenic-related genes, *Alp*, *Ocn*, and *Runx2*, were significantly upregulated

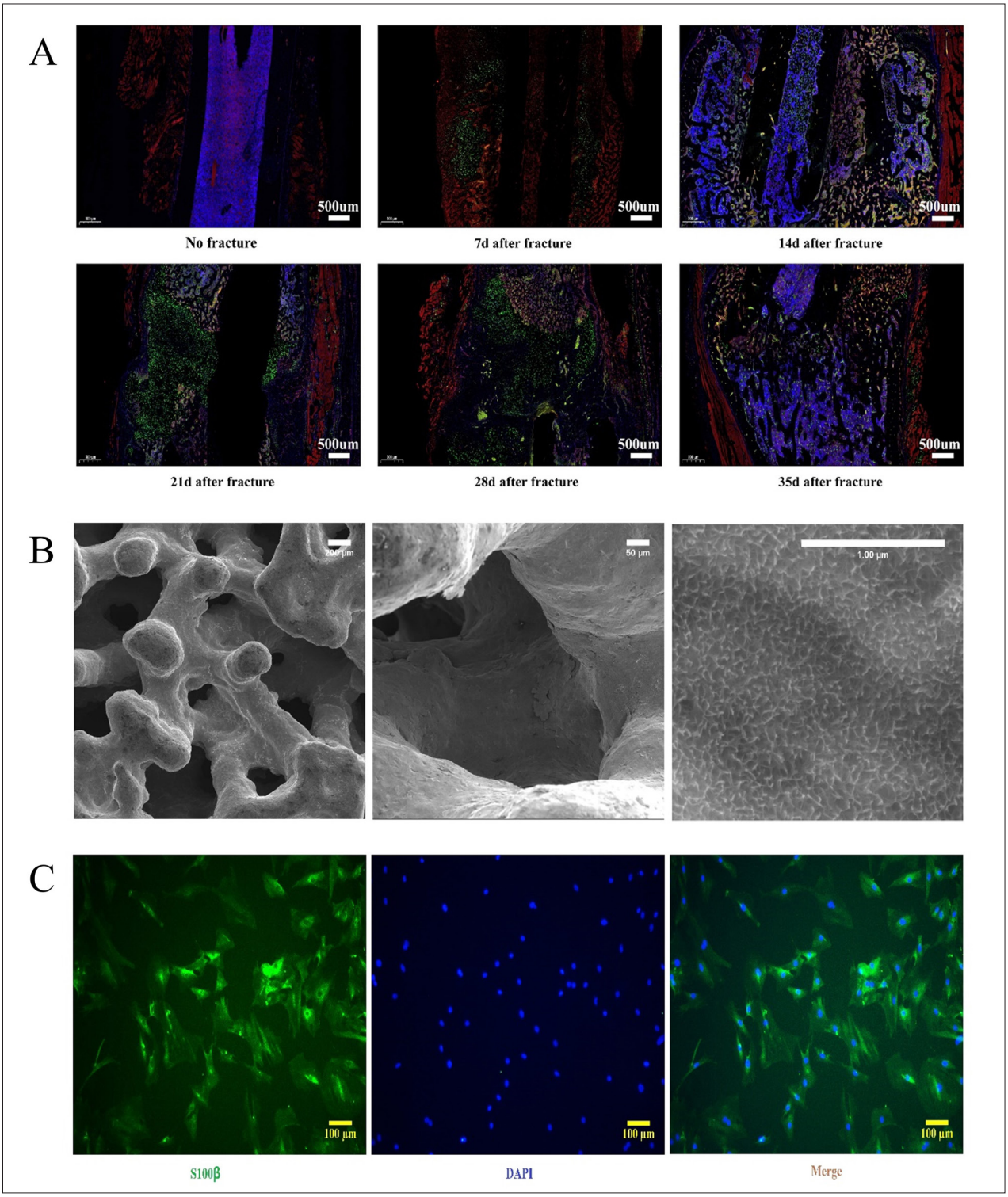

Figure 2. Observations of rat tibial immunofluorescence, scaffold surface morphology, and SCs identification. (A) Immunofluorescence staining of rat tibial specimens: red fluorescence represents nerve axons labeled with β III-tubulin; green fluorescence indicates SCs labeled with S100β; blue fluorescence marks nuclei stained with DAPI. Scale bar = 500 μm; Magnification = 40×. (B) Scanning electron microscopy images showing the surface morphology of the bionic trabecular titanium alloy scaffold. Scale bar = 1–200 μm; Magnifications = 100×, 400× and 10,000× (from left to right). (C) Identification of extracted SCs via immunofluorescence staining using S100β. Scale bar = 100 μm; Magnification = 200×. Abbreviations: DAPI, 4',6-diamidino-2-phenylindole; S100β, S100 calcium-binding protein B; SCs, Schwann cells.

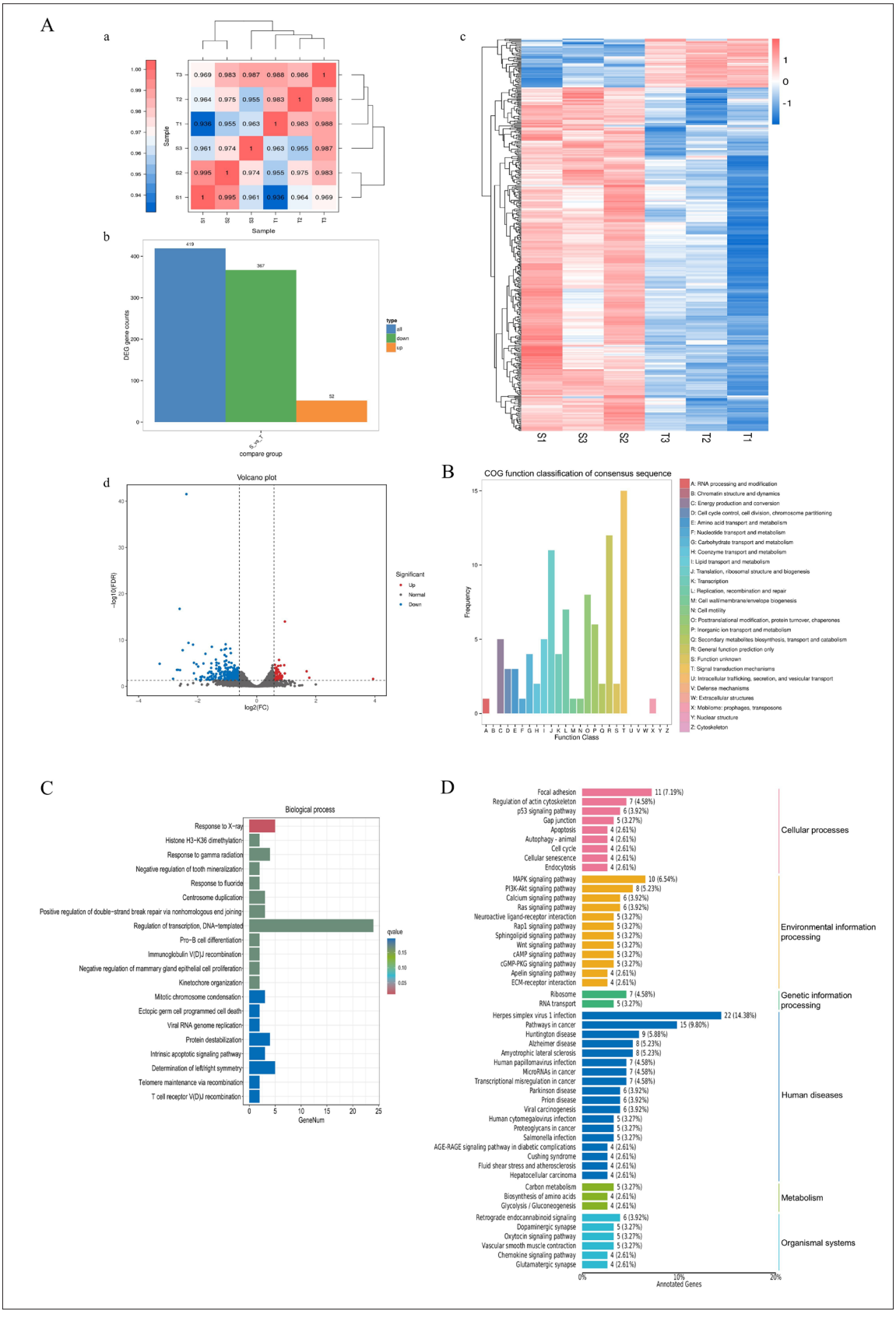
A
a
Sample
T3 0.969 0.983 0.987 0.988 0.986 1
T2 0.964 0.975 0.955 0.983 1 0.986
T1 0.936 0.955 0.963 1 0.983 0.988
S3 0.961 0.974 1 0.963 0.955 0.987
S2 0.995 1 0.974 0.955 0.975 0.983
S1 1 0.995 0.961 0.936 0.964 0.969
S1 S2 S3 T1 T2 T3
Sample
b
DEG gene counts
419
367
52
type
all
down
up
compare group
c
1
0
-1
S1 S3 S2 T3 T2 T1
d
Volcano plot
-log10(FDR)
log2(FC)
Significant
Up
Normal
Down
B
COG function classification of consensus sequence
Frequency
Function Class
A: RNA processing and modification
B: Chromatin structure and dynamics
C: Energy production and conversion
D: Cell cycle control, cell division, chromosome partitioning
E: Amino acid transport and metabolism
F: Nucleotide transport and metabolism
G: Carbohydrate transport and metabolism
H: Coenzyme transport and metabolism
I: Lipid transport and metabolism
J: Translation, ribosomal structure and biogenesis
K: Transcription
L: Replication, recombination and repair
M: Cell wall/membrane/envelope biogenesis
N: Cell motility
O: Posttranslational modification, protein turnover, chaperones
P: Inorganic ion transport and metabolism
Q: Secondary metabolites biosynthesis, transport and catabolism
R: General function prediction only
S: Function unknown
T: Signal transduction mechanisms
U: Intracellular trafficking, secretion, and vesicular transport
V: Defense mechanisms
W: Extracellular structures
X: Mobilome: prophages, transposons
Y: Nuclear structure
Z: Cytoskeleton
C
Biological process
Response to X-ray
Histone H3-K36 dimethylation
Response to gamma radiation
Negative regulation of tooth mineralization
Response to fluoride
Centrosome duplication
Positive regulation of double-strand break repair via nonhomologous end joining
Regulation of transcription, DNA-templated
Pro-B cell differentiation
Immunoglobulin V(D)J recombination
Negative regulation of mammary gland epithelial cell proliferation
Kinetochore organization
Mitotic chromosome condensation
Ectopic germ cell programmed cell death
Viral RNA genome replication
Protein destabilization
Intrinsic apoptotic signaling pathway
Determination of left/right symmetry
Telomere maintenance via recombination
T cell receptor V(D)J recombination
qvalue
GeneNum
D
Focal adhesion 11 (7.19%)
Regulation of actin cytoskeleton 7 (4.58%)
p53 signaling pathway 6 (3.92%)
Gap junction 5 (3.27%)
Apoptosis 4 (2.61%)
Autophagy - animal 4 (2.61%)
Cell cycle 4 (2.61%)
Cellular senescence 4 (2.61%)
Endocytosis 4 (2.61%)
MAPK signaling pathway 10 (6.54%)
PI3K-Akt signaling pathway 8 (5.23%)
Calcium signaling pathway 6 (3.92%)
Ras signaling pathway 6 (3.92%)
Neuroactive ligand-receptor interaction 5 (3.27%)
Rap1 signaling pathway 5 (3.27%)
Sphingolipid signaling pathway 5 (3.27%)
Wnt signaling pathway 5 (3.27%)
cAMP signaling pathway 5 (3.27%)
cGMP-PKG signaling pathway 5 (3.27%)
Apelin signaling pathway 4 (2.61%)
ECM-receptor interaction 4 (2.61%)
Ribosome 7 (4.58%)
RNA transport 5 (3.27%)
Herpes simplex virus 1 infection 22 (14.38%)
Pathways in cancer 15 (9.80%)
Huntington disease 9 (5.88%)
Alzheimer disease 8 (5.23%)
Amyotrophic lateral sclerosis 8 (5.23%)
Human papillomavirus infection 7 (4.58%)
MicroRNAs in cancer 7 (4.58%)
Transcriptional misregulation in cancer 7 (4.58%)
Parkinson disease 6 (3.92%)
Prion disease 6 (3.92%)
Viral carcinogenesis 6 (3.92%)
Human cytomegalovirus infection 5 (3.27%)
Proteoglycans in cancer 5 (3.27%)
Salmonella infection 5 (3.27%)
AGE-RAGE signaling pathway in diabetic complications 4 (2.61%)
Cushing syndrome 4 (2.61%)
Fluid shear stress and atherosclerosis 4 (2.61%)
Hepatocellular carcinoma 4 (2.61%)
Carbon metabolism 5 (3.27%)
Biosynthesis of amino acids 4 (2.61%)
Glycolysis / Gluconeogenesis 4 (2.61%)
Retrograde endocannabinoid signaling 6 (3.92%)
Dopaminergic synapse 5 (3.27%)
Oxytocin signaling pathway 5 (3.27%)
Vascular smooth muscle contraction 5 (3.27%)
Chemokine signaling pathway 4 (2.61%)
Glutamatergic synapse 4 (2.61%)
Cellular processes
Environmental information processing
Genetic information processing
Human diseases
Metabolism
Organismal systems
Annotated Genes

Figure 3. Transcriptomic sequencing and functional annotation. (A) Transcriptomic sequencing results: a. Correlation analysis of replicates; b. Bar chart of DEGs; c. Heatmap of gene expression clustering; d. Volcano plot of DEG expression. T represents the bionic trabecular group, and S represents the solid structure group. (B) COG classification of DEGs. (C) KEGG pathway annotation of DEGs. (D) Gene Ontology enrichment analysis of DEGs. Abbreviations: AGE, advanced glycation endproduct; Akt, protein kinase B; cAMP, cyclic adenosine monophosphate; cGMP, cyclic guanosine monophosphate; COG, cluster of orthologous genes; DEGs, differentially expressed genes; ECM, extracellular matrix; FC, fold-change; FDR, false discovery rate; KEGG, Kyoto Encyclopedia of Genes and Genomes; MAPK, mitogen-activated protein kinase; PI3K, phosphoinositide 3-kinase; PKG, protein kinase G; Ras, pat sarcoma virus; Rap1, Ras-proximate-1 or Ras-related protein 1; RAGE, receptor for advanced glycation endproducts.

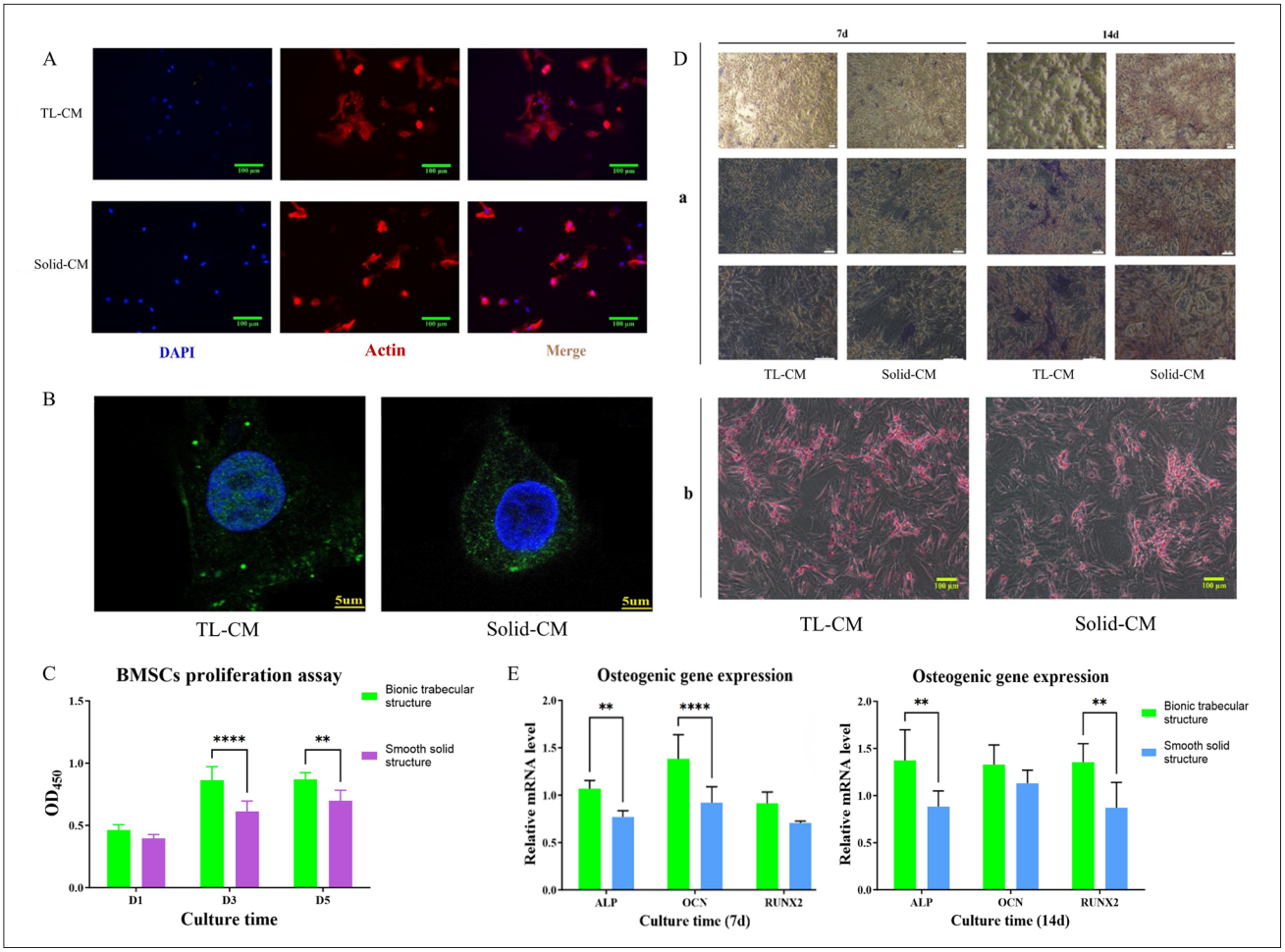

Figure 4. Morphological observation of SCs and functional analysis on titanium alloy scaffolds. (A) SCs on titanium alloy scaffolds. Phalloidin/DAPI staining shows a well-defined cytoskeleton and larger spreading area on the bionic trabecular scaffold compared to the solid scaffold. Scale bar = 100 μm; Magnification = 200×. (B) Nuclear localization of p-ERK (green) in SCs. Nuclei are stained with DAPI (blue). SCs on the bionic trabecular scaffold exhibit enhanced p-ERK nuclear localization. Scale bar = 5 μm; Magnification = 600×. (C) BMSC proliferation curve in SC-conditioned medium via Cell Counting Kit-8 assay. (D) Osteogenic differentiation of BMSCs. (a) ALP staining on day 7 and 14. Scale bar = 100 μm; Magnification = 100×. (b) Alizarin Red staining on day 30. Scale bar = 100 μm; Magnification = 200×. (E) mRNA expression of *Alp*, *Ocn*, and *Runx2* in BMSCs on day 7 and 14. *$p < 0.05$, TL-CM versus Solid-CM. Abbreviations: ALP, alkaline phosphatase; BMSCs, bone marrow-derived mesenchymal stem cells; DAPI, 4',6-diamidino-2-phenylindole; mRNA, messenger RNA; *Ocn*, osteocalcin; OD, optical density; p-ERK, phosphorylated extracellular signal-regulated kinases; *Runx2*, runt-related transcription factor 2; SCs, Schwann cells; Solid-CM, solid scaffold-conditioned medium; TL-CM, trabecular-like scaffold-conditioned medium.

in the TL-CM group compared to the Solid-CM group ($p < 0.05$) (Figure 4E).

3.7. Angiogenesis assay

Endothelial cells cultured on Matrigel formed tubular structures, demonstrating robust angiogenesis. Under an optical microscope (10×), the cells were observed to arrange into a branched, network-like structure. Quantitative analysis using the Angiogenesis Analyzer plugin in ImageJ showed a significant increase in the number of nodes in the bionic trabecular titanium alloy scaffold-treated group compared to the smooth solid titanium alloy scaffold group ($p < 0.05$). Furthermore, the number of junctions formed was significantly higher in the SC-conditioned medium derived from the bionic trabecular titanium alloy scaffold group ($p < 0.05$). The results are shown in Figure 5A and 5C.

3.8. Endothelial cell migration assay

In the scratch wound healing assay, all treatment groups exhibited varying degrees of endothelial cell migration at 12 and 24 h. Quantitative analysis of the scratch area using ImageJ was used to calculate the scratch healing rate. At 12 h, the healing rate in the SC-conditioned medium derived from the bionic trabecular titanium alloy scaffold group was 28.32 ± 2.74%, significantly higher than that of the smooth solid titanium alloy scaffold group (11.02 ± 1.10%) ($p < 0.05$). At 24 h, the healing rate increased to 49.35 ± 7.96% in the bionic trabecular titanium alloy scaffold group, compared to 27.38±2.03% in the smooth solid titanium alloy scaffold group ($p < 0.05$). The results are shown in Figure 5B and 5D.

3.9. ELISA assay

The expression levels of BDNF, NGF, and PDGF-AA were measured in the bionic trabecular group, solid scaffold group, and the blank control group using ELISA. The results showed that the bionic trabecular group exhibited significantly higher levels of BDNF, NGF, and PDGF-AA compared to both the solid scaffold group and the blank control group ($p < 0.05$). Statistical analysis indicates that the bionic trabecular group enhances the secretion of neurotrophic factors, potentially contributing to an improved bone repair microenvironment. The results are shown in Figure 5E.

4. Discussion

Titanium alloys have long been established as a cornerstone in orthopedic applications due to their excellent mechanical properties and biocompatibility.[15,16] However, their high elastic modulus, which significantly exceeds that of natural bone, often leads to the stress shielding phenomenon, resulting in bone resorption and implant loosening, particularly in osteoporotic patients.[17,18] Furthermore, their bioinert nature limits their ability to integrate with bone.[19] Addressing these limitations, our study explored the development and application of bionic trabecular titanium alloy scaffolds with a micro–nano composite porous structure. By mimicking the trabecular architecture of cancellous bone, these scaffolds provide both mechanical adaptability and enhanced biological functionality, laying a promising foundation for improved bone defect repair.[20,21] The elastic modulus of a material plays a crucial role in the mechanical compatibility between the implant and surrounding bone tissue. Traditional titanium alloys used in orthopedic implants have a high elastic modulus of approximately 110 GPa, which is significantly greater than that of natural cortical bone (17–20 GPa) and cancellous bone (~4 GPa).[22] This discrepancy leads to the stress shielding phenomenon, where the implant bears most of the mechanical load, resulting in reduced bone remodeling and eventual bone resorption. To address this issue, our study focused on the use of bionic trabecular titanium alloy scaffolds, which reduce the elastic modulus to approximately 4 GPa, more closely matching that of cancellous bone. This reduction in elastic modulus minimizes the stress-shielding effect, thereby promoting better bone-implant integration and reducing the risk of implant failure. Mechanical testing conducted on our scaffolds demonstrated that the bionic trabecular scaffolds exhibited improved load-bearing capacity compared to solid titanium alloys while reducing stress concentration at the bone–implant interface. *In vitro* experiments further validated that scaffolds with reduced elastic modulus enhanced osteogenesis, as evidenced by increased ALP activity and mineralized nodule formation, indicating improved bone formation at the implant site. These findings support the hypothesis that reducing the elastic modulus of titanium implants can alleviate stress

Figure 5. Angiogenesis, scratch assay, and factor expression in different titanium alloy scaffolds. (A) Angiogenesis assay observed under an optical microscope (10× magnification). (B) Scratch wound healing assay observed under an optical microscope (5× magnification). (C) Scratch healing rates: a. at 12 h; b. at 24 h. (D) Angiogenesis quantification: a. Nb nodes; b. Nb junctions; c. total master segment length. (E) Expression levels of secreted factors: a. BDNF; b. NGF; c. PDGF-AA. Abbreviations: BDNF, brain-derived neurotrophic factor; Nb junctions, number of junctions; Nb nodes, number of nodes; NGF, nerve growth factor; PDGF-AA, platelet-derived growth factor with two A subunits; Solid-CM, solid scaffold-conditioned medium; TL-CM, trabecular-like scaffold-conditioned medium.

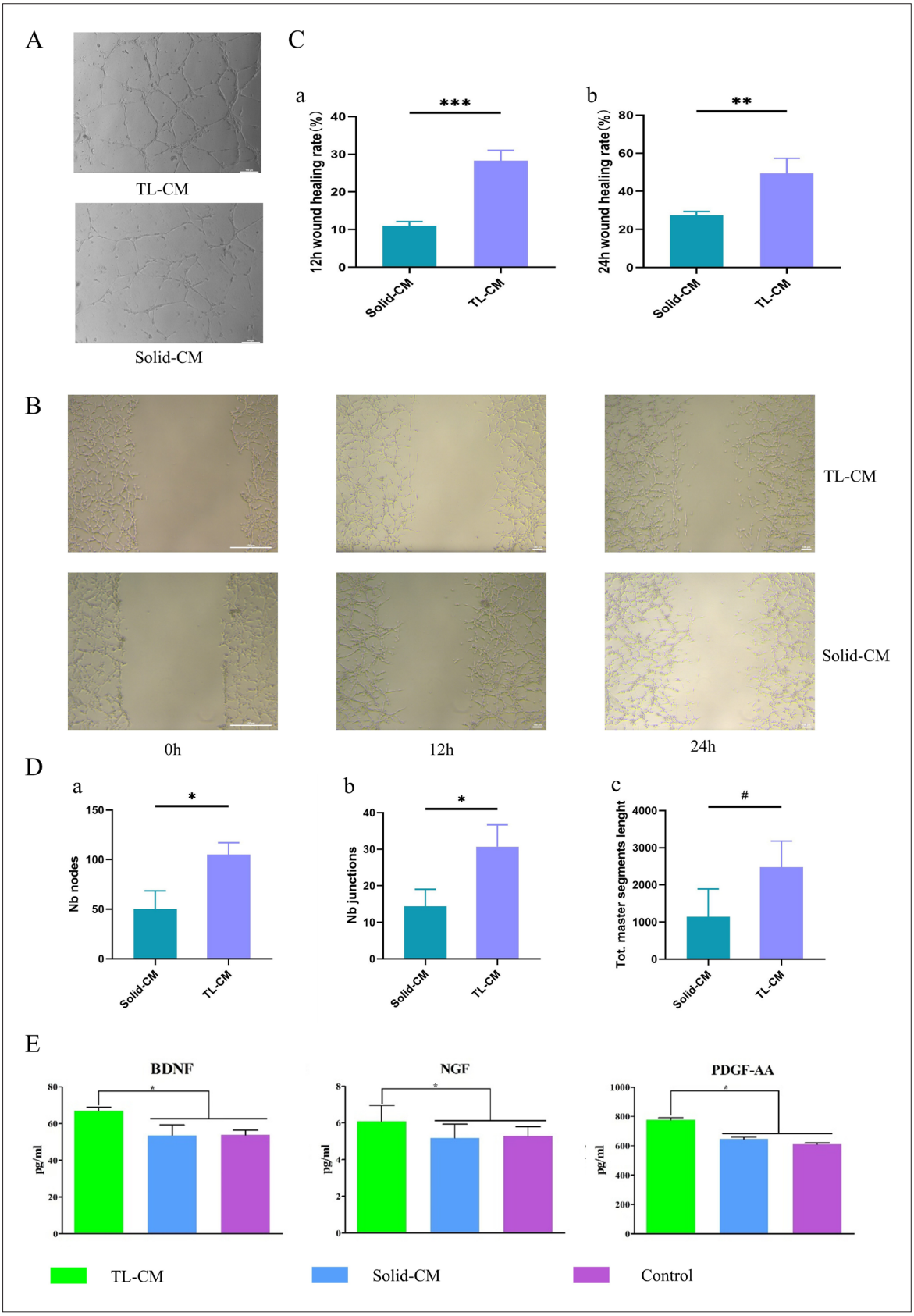
A
TL-CM
Solid-CM
C
a
***
12h wound healing rate (%)
Solid-CM
TL-CM
b
**
24h wound healing rate (%)
Solid-CM
TL-CM
B
TL-CM
Solid-CM
0h
12h
24h
D
a
*
Nb nodes
Solid-CM
TL-CM
b
*
Nb junctions
Solid-CM
TL-CM
c
#
Tot. master segments lenght
Solid-CM
TL-CM
E
BDNF
NGF
PDGF-AA
pg/ml
TL-CM
Solid-CM
Control

shielding and enhance osseointegration, leading to more stable and functional implants in clinical applications.

Importantly, this study extends beyond traditional material-bone cell interactions by incorporating the regulatory role of SCs into the scaffold-guided repair paradigm. SCs cultured on bionic trabecular scaffolds exhibited enhanced adhesion and elongation, forming spindle-shaped morphologies along the scaffold's microporous structures. This is likely due to the increased surface roughness, curvature, and nanopores, which provided more adhesion points and stimulated cellular responses.[23,24] In contrast, SCs on smooth solid scaffolds displayed a flatter morphology, with limited cell elongation and intercellular connections. These findings highlight the importance of surface morphology in influencing SC behavior.[25]

Mechanistically, our study suggests that the bionic trabecular scaffolds modulate SC function through mechanotransduction pathways, specifically the FAK-MAPK signaling axis. This pathway converts mechanical stimuli from the scaffold into intracellular signals, leading to downstream gene expression and enhanced cellular functions.[26] This mechanosensitive response is critical for the upregulation of neurotrophic and osteogenic factors such as BDNF, NGF, and PDGF-AA, which were significantly increased in SCs grown on bionic scaffolds.[27,28] These factors, in turn, orchestrate downstream osteogenesis and angiogenesis, thus contributing to a favorable microenvironment for bone repair.

The conditioned medium derived from SCs on bionic scaffolds (TL-CM) further confirmed the scaffold's ability to stimulate paracrine signaling. TL-CM enhanced BMSC proliferation, ALP activity, calcium deposition, and the expression of osteogenic genes (*Alp*, *Ocn*, and *Runx2*), indicating a robust osteoinductive effect. Moreover, endothelial cell assays revealed improved tube formation and migration under TL-CM treatment, suggesting that SC-derived angiogenic factors also play a vital role in vascular support during bone regeneration.[29]

Compared to conventional surface treatments such as sandblasting, acid etching, or hydroxyapatite coating, the bionic trabecular design offers dual benefits: biomechanical compatibility and biologically active surface cues. While traditional modifications improve initial cell adhesion, they fail to address elastic mismatch or regulate advanced cellular behaviors through mechanosensitive pathways.[5] The biomimetic design of the bionic trabecular scaffold not only reduces stress shielding through biomechanical adaptation but also enhances bioactivity by regulating cell behavior via surface morphology.[30] These findings align with previous studies emphasizing the importance of porous structures in improving the mechanical and biological properties of biomaterials.[31,32]

Despite the promising results, our study intentionally focused on *in vitro* models to isolate the specific contributions of SCs to bone regeneration. *In vivo* environments involve complex systemic interactions, such as immune responses, vascular remodeling, and multicellular crosstalk, which may obscure the scaffold's SC-specific effects.[12] Future studies should adopt co-culture or organoid models to better simulate the multicellular complexity of the bone niche. Moreover, while our data implicate FAK-MAPK signaling, further investigation is needed to dissect its downstream targets and interactions with other mechanosensitive pathways (e.g., Yes-associated protein/transcriptional co-activator with a PDZ-binding domain, integrin-linked kinase) in SC-mediated repair. Additionally, the independent contributions of surface curvature, nanopore size, and chemical treatment require further clarification through the use of gradient-designed scaffold systems.[33]

In summary, this study demonstrates that bionic trabecular titanium alloy scaffolds with micro–nano composite porous structures promote SC function via FAK-MAPK-mediated mechanotransduction. This, in turn, enhances the secretion of neurotrophic and osteogenic factors, thereby stimulating osteogenesis and angiogenesis within the bone repair microenvironment. By bridging neural regulation and materials science, this work provides a novel theoretical and practical foundation for neural-assisted bone tissue engineering. Future research incorporating multicellular and *in vivo* models will further facilitate the clinical translation of this approach.[34]

5. Conclusion

Our experiments demonstrate that bionic trabecular titanium alloy scaffolds with a micro–nano composite porous structure exhibit significant potential in promoting the bone and vascular formation and enhancing osseointegration, providing new insights and solutions for bone defect repair. Future studies could integrate this scaffold design with patient-specific metal 3D printing (e.g., SLM), distinct from biological 3D printing involving living cells, to address complex bone defects by leveraging the flexibility of 3D printing for customized solutions.

Acknowledgments

The authors thank the technical staff at Xi'an Jiaotong University for their assistance with scaffold fabrication and cell culture.

Funding

This work was supported by grants from the ShaanxiNatural Science Basic Research Foundation (No. 2024JC-YBQN-0964), the Xi'an Science and Technology Plan Project (No. 22YXYJ0032), the Shaanxi Health and Family Planning Commission (No. 2017SF-087, 2021SF-170, and 2022E001), and the Xi'an Central Hospital Project (No. 2023ZD002).

Conflict of interest

The authors declare no competing financial or non-financial interests.

Author contributions

Conceptualization: Jiqing Wang, Aofei Xu
Data curation: Weiying Zhang, Xingda Huang
Formal analysis: Weiying Zhang, Xingda Huang
Funding acquisition: Dezhi Wang, Jiantao Liu
Investigation: Xuezhe Han, Shuming Li
Methodology: Jiqing Wang, Aofei Xu
Supervision: Dezhi Wang, Jiantao Liu
Visualization: Xuezhe Han, Shuming Li
Writing – original draft: Jiqing Wang, Aofei Xu
Writing – review & editing: Dezhi Wang, Jiantao Liu

Ethical approval and consent to participate

All animal experiments were conducted in accordance with institutional guidelines and were approved by the Ethics Committee of Xi'an Jiaotong University (approval number: XJTUAE2024-625).

Consent for publication

Not applicable.

Availability of data

The datasets generated and analyzed during this study are available from the corresponding authors upon reasonable request.

References

1. Clynes MA, Harvey NC, Curtis EM, Fuggle NR, Dennison EM, Cooper C. The epidemiology of osteoporosis. *Br Med Bull*. 2020;133(1):105-117.
doi: 10.1093/bmb/ldaa005

2. Beird HC, Bielack SS, Flanagan AM, et al. Osteosarcoma. *Nat Rev Dis Primers*. 2022;8(1):77.
doi: 10.1038/s41572-022-00409-y

3. Shi Y, Liu J, Du M, et al. Customized barrier membrane (titanium alloy, poly ether-ether ketone and unsintered hydroxyapatite/poly-l-lactide) for guided bone regeneration. *Front Bioeng Biotechnol*. 2022;10:916967.
doi: 10.3389/fbioe.2022.916967

4. Rout PK, Roy S, Ganguly S, Rathore DK. A review on properties of magnesium-based alloys for biomedical applications. *Biomed Phys Eng Express*. 2022;8(4):042002.
doi: 10.1088/2057-1976/ac6d81

5. Jiang P, Zhang Y, Hu R, et al. Advanced surface engineering of titanium materials for biomedical applications: From static modification to dynamic responsive regulation. *Bioact Mater*. 2023;27:15-57.
doi: 10.1016/j.bioactmat.2023.03.006

6. Li J, Zheng Y, Yu Z, et al. Surface-modified titanium and titanium-based alloys for improved osteogenesis: a critical review. *Heliyon*. 2024;10(1):e23779.
doi: 10.1016/j.heliyon.2023.e23779

7. Liu B, Wang H, Zhang N, Zhang M, Cheng CK. Femoral stems with porous lattice structures: a review. *Front Bioeng Biotechnol*. 2021;9:772539.
doi: 10.3389/fbioe.2021.772539

8. Zhang B, Li J, He L, Huang H, Weng J. Bio-surface coated titanium scaffolds with cancellous bone-like biomimetic structure for enhanced bone tissue regeneration. *Acta Biomater*. 2020;114:431-448.
doi: 10.1016/j.actbio.2020.07.024

9. Ziaie B, Velay X, Saleem W. Advanced porous hip implants: a comprehensive review. *Heliyon*. 2024;10(18):e37818.
doi: 10.1016/j.heliyon.2024.e37818

10. Hou C, An J, Zhao D, et al. Surface modification techniques to produce micro/nano-scale topographies on Ti-based implant surfaces for improved osseointegration. *Front Bioeng Biotechnol*. 2022;10:835008.
doi: 10.3389/fbioe.2022.835008

11. Salhotra A, Shah HN, Levi B, Longaker MT. Mechanisms of bone development and repair. *Nat Rev Mol Cell Biol*. 2020;21(11):696-711.
doi: 10.1038/s41580-020-00279-w

12. Damiati LA, El Soury M. Bone-nerve crosstalk: a new state for neuralizing bone tissue engineering–a mini review. *Front Med (Lausanne)*. 2024;11:1386683.
doi: 10.3389/fmed.2024.1386683

13. Yuan Q, Liao D, Yang X, et al. Effect of implant surface microtopography on proliferation, neurotrophin secretion, and gene expression of Schwann cells. *J Biomed Mater Res A*. 2010;93(1):381-8.
doi: 10.1002/jbm.a.32548

14. Wang YY, Gong P, Zhang J. Effects of different implant surface properties on the biological behavior of Schwann cells. *Hua Xi Kou Qiang Yi Xue Za Zhi*. 2021;39(3):279-285.
doi: 10.7518/hxkq.2021.03.006

15. Jing Z, Zhang T, Xiu P, et al. Functionalization of 3D-printed titanium alloy orthopedic implants: a literature review. *Biomed Mater*. 2020;15(5):052003. doi: 10.1088/1748-605X/ab9078

16. Fan L, Chen S, Yang M, Liu Y, Liu J. Metallic materials for bone repair. *Adv Healthc Mater*. 2024;13(3):e2302132. doi: 10.1002/adhm.202302132

17. Gao X, Zhao Y, Wang M, Liu Z, Liu C. Parametric design of hip implant with gradient porous structure. *Front Bioeng Biotechnol*. 2022;10:850184. doi: 10.3389/fbioe.2022.850184

18. Arias-González F, Rodríguez-Contreras A, Punset M, et al. Laser-Deposited beta type Ti-42Nb alloy with anisotropic mechanical properties for pioneering biomedical implants with a very low elastic modulus. *Materials (Basel)*. 2022;15(20):7172. doi: 10.3390/ma15207172

19. Yang S, Jiang W, Ma X, et al. Nanoscale morphologies on the surface of 3D-printed titanium implants for improved osseointegration: a systematic review of the literature. *Int J Nanomedicine*. 2023;18:4171-4191. doi: 10.2147/ijn.S409033

20. Gu Y, Sun Y, Shujaat S, Braem A, Politis C, Jacobs R. 3D-printed porous Ti6Al4V scaffolds for long bone repair in animal models: a systematic review. *J Orthop Surg Res*. 2022;17(1):68. doi: 10.1186/s13018-022-02960-6

21. Shao H, Zhang Q, Sun M, et al. Effects of hydroxyapatite-coated porous titanium scaffolds functionalized by exosomes on the regeneration and repair of irregular bone. *Front Bioeng Biotechnol*. 2023;11:1283811. doi: 10.3389/fbioe.2023.1283811

22. Niinomi M, Liu Y, Nakai M, Liu H, Li H. Biomedical titanium alloys with Young's moduli close to that of cortical bone. *Regen Biomater*. 2016;3(3):173-85. doi: 10.1093/rb/rbw016

23. Dai Y, Lu T, Li L, et al. Electrospun composite PLLA-PPSB nanofiber nerve conduits for peripheral nerve defects repair and regeneration. *Adv Healthc Mater*. 2024; 13(10):e2303539. doi: 10.1002/adhm.202303539

24. Li X, He N, Li X, et al. Graphdiyne-loaded polycaprolactone nanofiber scaffold for peripheral nerve regeneration. *J Colloid Interface Sci*. 2023;646:399-412. doi: 10.1016/j.jcis.2023.05.054

25. da Silva VA, Bobotis BC, Correia FF, et al. The impact of biomaterial surface properties on engineering neural tissue for spinal cord regeneration. *Int J Mol Sci*. 2023; 24(17):13642. doi: 10.3390/ijms241713642

26. Wang Z, Zhao Y, Bai H, et al. Bioactive prosthesis interface compositing variable-stiffness hydrogels regulates stem cells fates to facilitate osseointegration through mechanotransduction. *Int J Biol Macromol*. 2024; 259(Pt 2):129073. doi: 10.1016/j.ijbiomac.2023.129073

27. Park EJ, Truong VL, Jeong WS, Min WK. Brain-derived neurotrophic factor (BDNF) enhances osteogenesis and may improve bone microarchitecture in an ovariectomized rat model. *Cells*. 2024;13(6):518. doi: 10.3390/cells13060518

28. Fitzpatrick V, Martín-Moldes Z, Deck A, et al. Functionalized 3D-printed silk-hydroxyapatite scaffolds for enhanced bone regeneration with innervation and vascularization. *Biomaterials*. 2021;276:120995. doi: 10.1016/j.biomaterials.2021.120995

29. Wu Z, Pu P, Su Z, Zhang X, Nie L, Chang Y. Schwann cell-derived exosomes promote bone regeneration and repair by enhancing the biological activity of porous Ti6Al4V scaffolds. *Biochem Biophys Res Commun*. 2020;531(4):559-565. doi: 10.1016/j.bbrc.2020.07.094

30. Wei X, Zhou W, Tang Z, et al. Magnesium surface-activated 3D printed porous PEEK scaffolds for in vivo osseointegration by promoting angiogenesis and osteogenesis. *Bioact Mater*. 2023;20:16-28. doi: 10.1016/j.bioactmat.2022.05.011

31. Choudhary R, Bulygina I, Lvov V, et al. Mechanical, structural, and biological characteristics of polylactide/wollastonite 3D printed scaffolds. *Polymers (Basel)*. 2022;14(19):3932. doi: 10.3390/polym14193932

32. Ait Said H, Mabroum H, Lahcini M, et al. Manufacturing methods, properties, and potential applications in bone tissue regeneration of hydroxyapatite-chitosan biocomposites: a review. *Int J Biol Macromol*. 2023; 243:125150. doi: 10.1016/j.ijbiomac.2023.125150

33. Zhang Z, Lv Y, Harati J, et al. Submicron-grooved films modulate the directional alignment and biological function of schwann cells. *J Funct Biomater*. 2023;14(5):238. doi: 10.3390/jfb14050238

34. Kong D, Wang Q, Huang J, et al. Design and manufacturing of biomimetic scaffolds for bone repair inspired by bone trabeculae. *Comput Biol Med*. 2023;165:107369. doi: 10.1016/j.compbiomed.2023.107369